Journal of Nuclear Materials 442 (2013) S142–S147
DOI:http://dx.doi.org/10.1016/j.jnucmat.2012.11.001

Microstructure and tensile properties of oxide dispersion strengthened Fe–14Cr–$0.3Y_2O_3$ and Fe–14Cr–2W–0.3Ti–$0.3Y_2O_3$

M.A. Auger *, V. de Castro, T. Leguey, M.A. Monge, A. Muñoz, R. Pareja

Departamento de Física, Universidad Carlos III de Madrid, 28911 Leganés, Spain

Abstract: Two ODS ferritic steels with nominal compositions (wt.%): Fe 14Cr $0.3Y_2O_3$ and Fe 14Cr 2W 0.3Ti $0.3Y_2O_3$ have been produced by mechanical alloying and consolidation by hot isostatic pressing. The microstructure and tensile properties of these materials after being forged and heat treated at 1123 K have been investigated to clarify the interrelation between composition, microstructure and mechanical properties. The second phase precipitates in these alloys have been analyzed by high angle annular dark field imaging in scanning TEM mode and electron diffraction. Fe 14Cr 2W 0.3Ti $0.3Y_2O_3$ exhibits a duplex microstructure consisting of large recrystallized grains, as large as 1.5 μm, and unrecovered regions containing submicron equiaxed grains. In addition, three types of secondary phase particles have been found: large $M_{23}C_6$ particles containing W and Cr, (Cr + Ti) rich spherical particles with diameters between 50 and 500 nm, and fine (Y + Ti) oxide particles with sizes below 30 nm. In contrast, Fe14CrY shows a uniform structure of equiaxed grains, with sizes in the range 0.5 3 μm, containing a fine disper sion of Y oxide particles (<30 nm) homogeneously distributed inside the grains, as well as large carbide and oxide particles. Tensile tests performed over the temperature range 273 973 K have revealed that the alloy containing W and Ti has lower yield and tensile strengths than Fe 14Cr $0.3Y_2O_3$ at tempera tures up to 773 K, but the opposite appears to occur beyond this temperature.

1. Introduction

Irradiation resistance, high temperature strength, creep resis tance and reduced activation are the main properties required in the structural materials that will be used to build power fusion reactors with enhanced efficiency and safety. Among the possible structural materials for fusion devices, oxide dispersion strength ened (ODS) ferritic steels with reduced activation appear to be very promising candidates [1 6]. The increasing interest in developing nano structured ODS and reduced activation ferritic (RAF) steels relies on experimental results that have shown their enhanced irradiation resistance, high temperature properties and thermal stability. The microstructural characteristics of these ODS RAF steels, which depend on the composition and processing condi tions, are key for getting the desired improved properties. Among the ODS RAF steels investigated, those of composition Fe 14Cr 2W $0.3Y_2O_3$ (wt.%) with Ti addition appear to exhibit the most favorable microstructure for achieving improved mechanical behavior at elevated temperatures [7 11]. The purpose of the work presented here was to compare the microstructure and tensile properties of an ODS Fe 14Cr steel with those for an ODS Fe 14Cr 2W 0.3Ti steel processed at similar conditions to clarify the relationship between composition, microstructure and mechanical properties.

2. Experimental procedure

Two blends of elemental powders and nanosized Y_2O_3 powder with target compositions Fe 14%Cr 0.3%Y_2O_3 and Fe 14%Cr 2%W 0.3%Ti 0.3%Y_2O_3 (wt.%) (hereafter referred to as Fe14CrY and Fe14CrYWTi, respectively) were mechanically alloyed in a planetary ball mill under hydrogen atmosphere. The starting ele mental powders from Alfa Aesar had a purity and particle sizes, respectively, of 99.7% and <10 μm for Fe, 99.8% and <10 μm for Cr, 99.9% and <5 μm for W, and 99.8% and < 100 μm for Ti. The starting Y_2O_3 powder supplied by Nanophase Technologies was 99.5% pure in monoclinic phase with particle sizes $\leqslant$ 30 nm. The blends were mechanically alloyed in a planetary ball mill under hydrogen atmosphere. They were milled for 48 60 h at 300 rpm in 12% Cr steel vessels of 500 cm^3 of capacity using 10 mm ∅ chromium steel balls as grinding media at a ball to powder ratio of 10:1. Fig. 1 shows the morphology of the milled powders. Most of the particles were round or almost round, but elongated or pla ted shapes were also found. The mean particle sizes are 32 μm for the Fe14CrY milled powder and 23 μm for the Fe14CrYWTi milled

* Corresponding author. Tel.: +34 916249184; fax: +34 916248749.
E-mail address: mauger@fis.uc3m.es (M.A. Auger).

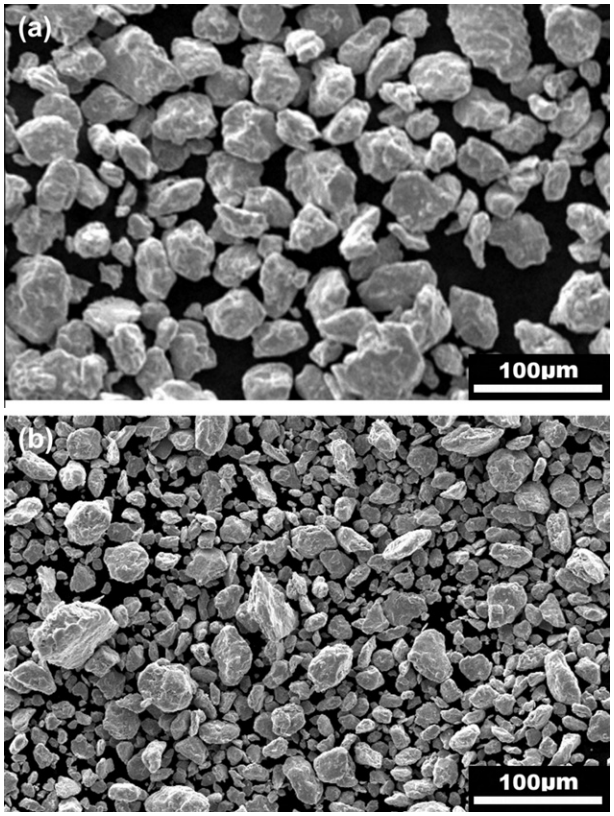

Fig. 1. SEM images of the (a) Fe14CrY and (b) Fe14CrYWTi milled powders.

powder. The backscattered electron images and the analyses of energy dispersive X ray spectroscopy (EDS) from the milled powder gave evidence of a homogeneous composition through the powder samples. X ray diffraction (XRD) measurements were also performed on samples of the milled powders. XRD patterns from the milled powders shown in Fig. 2a were consistent with a single ferrite phase with a lattice parameter of 2.871 ± 0.005 Å irre spective of the composition, i.e. 0.42% higher than the lattice parameter for bcc Fe. The O and C contents in samples of milled powders were quantified using TC500 and CS600 LECO analyzers. The O content in the milled powders ranged between 0.43 and 0.78 wt.% against contents of 0.32 0.37 wt.% in the initial powder blends. The C content was ~0.06 wt.% against values of 0.02 0.03 wt.% in the initial powder blends.

The milled powders were canned in 304L stainless steel con tainers (42 mm × 57 mm), degassed for 24 h at 823 K in vacuum (<10 ^{1} Pa), and then the containers were vacuum sealed. All the manipulation steps of the powders were carried out under an Ar atmosphere inside a glovebox. The canned powder was consoli dated by hot isostatic pressing (HIP) for 2 h at 1373 K and 200 MPa. The consolidated billet of the Fe14CrY alloy was forged at ~1373 K to shape a bar with dimensions ~12 mm × 12 mm × 179 mm. The Fe14CrYWTi billet had to be forged at ~1423 K in order to achieve a bar with the same dimensions. Then, the forged materials were heat treated for 2 h at 1123 K and air cooled. Final ly, the container was removed from the bars and their surfaces ground. Samples for microstructural analyses and mechanical characterization were cut using a SiC disk, or machined by elec tro erosion, and then properly polished.

Density measurements were performed on the alloys after the heat treatment using a He ultrapycnometer. The obtained values were: 7.48 ± 0.18 g/cm^3 for Fe14CrY and 7.73 ± 0.02 g/cm^3 for Fe14CrYWTi. The XRD patterns of the consolidated alloys after the heat treatment shown in Fig. 2b exhibit a slight variation of the lattice parameter, i.e. 2.865 ± 0.008 Å for Fe14CrY and 2.879 ± 0.001 Å for Fe14CrYWTi respect to the common value of 2.871 ± 0.005 Å for the alloyed powders. The changes in the widths of the XRD pattern peaks of the alloyed powders and the alloys after the heat treatment reflect changes in the crystallite sizes of the samples. The average crystallite sizes, estimated from the widths of the peaks by the Scherrer formula, result in 7 nm for the alloyed powders against ~20 nm for the consolidated alloys after being forged and heat treated.

General scanning transmission electron microscopy, (S)TEM, observations were carried out in a Philips CM20 microscope equipped with an EDS microanalysis system. A JEOL 3000F TEM microscope operated at 297 kV equipped with a detector for high angle annular dark field (HAADF) imaging in (S)TEM mode was used for the detailed analyses of the smaller second phase particles and for obtaining EDS elemental maps. To determine the crystalline structure of the second phase particles, the electron microdiffraction patterns were analyzed using the CaRine crystal lography software and structure data extracted from the Chemical Data Service [12]. From the crystallography analyses an indexing uncertainty for the experimental diffraction pattern is obtained. This uncertainty is defined as the average relative deviation of the interplanar distances measured on the pattern respect to corre sponding distances for the particular structures reported in the database. Samples for TEM, cut perpendicular to the axis of the bars, were thinned by electro polishing in a twin jet device using 5% $HClO_4$ + 95% CH_3OH as electrolyte. The Y rich nanoparticles

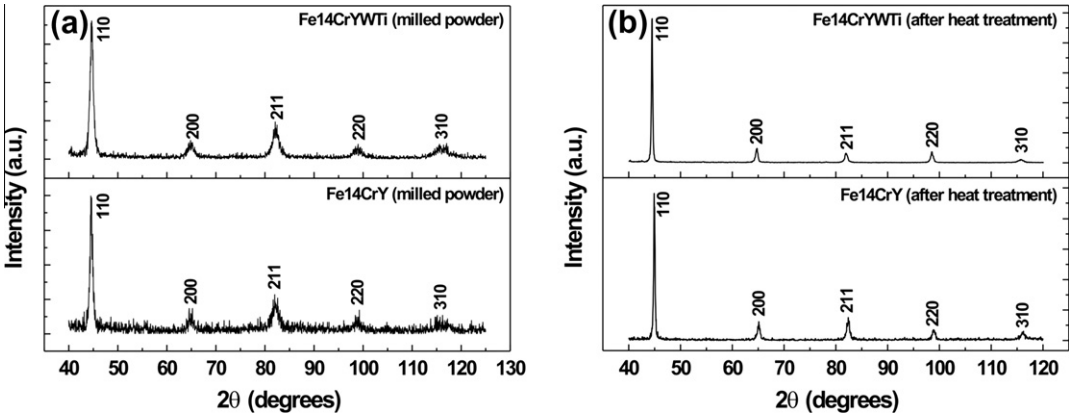

Fig. 2. XRD patterns for Fe14CrY and Fe14CrYWTi: (a) milled powders and (b) the consolidated alloys after heat-treatment.

number densities were measured on TEM foils in volumes of the order of 10 ^{20} m^3. The foil thickness was calculated using the log ratio technique, where the inelastic mean free path was estimated from the formula derived by Malis et al. [13]. Tensile tests in the temperature range 298 973 K at a constant crosshead rate of 0.1 mm/min were performed on flat tensile specimens with 20 mm gauge length × 3 mm width × 1 mm thickness cut parallel to the bar axis. Above room temperature, the tests were performed with the specimens under a flow of pure Ar to minimize the surface oxidation.

3. Results and discussion

3.1. Microstructural characterization

3.1.1. Fe14CrY

Fig. 3a shows TEM images of the microstructure observed in the heat treated Fe14CrY alloy. This alloy exhibited a uniform grain structure consisting of equiaxed grains with sizes in the range 0.5 3 μm as shown in Fig. 3a. Fig. 4 reveals that, inside the grains, a fine dispersion of second phase precipitates was visible, with mean diameters of 8 ± 6 nm and sizes smaller than ∼30 nm. Beside this dispersion of nanoparticles, Fig. 5a shows another uniform dis persion of particles with larger sizes, morphology somewhat differ ent and a Cr rich composition, as revealed in the STEM EDS elemental map image shown in Fig. 5b. These Cr rich particles had sizes between ∼0.2 and 1 μm and similar crystal structures than the two types of Cr rich particles found in the Fe14CrYWTi alloy. They were identified either as Cr_2O_3 oxides or $M_{23}C_6$ (M = Cr, Fe) carbides.

In contrast to the above Cr rich particles, the particles with si zes < 30 nm had an Y rich composition as the EDS elemental maps in Fig. 4a show. These Y rich nanoparticles are clearly differenti ated from the Cr rich particles when they are embedded into Cr rich particles or are very close to each other, as revealed from the elemental maps in Fig. 4b. Some particle could be indexed as orthorhombic $YCrO_3$ with uncertainties of <10%, but others could not be identified using FFT analyses. The mean number density of these Y rich nanoparticles was $(5 \pm 1) \times 10^{22}$ cm ^{3}. Few regions had lower values, of the order of 10^{21} cm ^{3}.

The quantitative EDS analyses in the matrix yield an average composition of 86.4% Fe and 13.4% Cr (wt.%), which is very accurate to the target composition of the alloy.

3.1.2. Fe14CrYWTi

A general view of this material is shown in Fig. 3b. A duplex grain structure containing large recovered grains and small unre covered submicron grains is visible. Fig. 6a and b shows the three types of second phase particles found that are discriminated by their number density, morphology, size and composition.

Type 1 These particles were the less numerous, with unde fined shapes and large sizes, and distributed no homogeneously are shown, labeled as 1, in Fig. 6a. They exhibited sizes up to ∼1.5 μm and were found associated to grain boundaries as well as inside the matrix grains. The microdiffraction patterns from sev eral Type 1 particles, with different orientations respect the elec tron beam, could be indexed as $M_{23}C_6$ (M = Cr, W, Fe) carbides with uncertainties of 8 12%. An example is shown in Fig. 6c.

Type 2 These particles, with a round shape and sizes between ∼50 and 500 nm, are distributed preferentially inside the matrix grains and more abundant than the Type 1 particles, as Fig. 6a and b shows labeled as 2. The EDS elemental mapping images of these particles shown in Fig. 7 reveal that these particles contain Cr and Ti, but no Fe, W or Y.

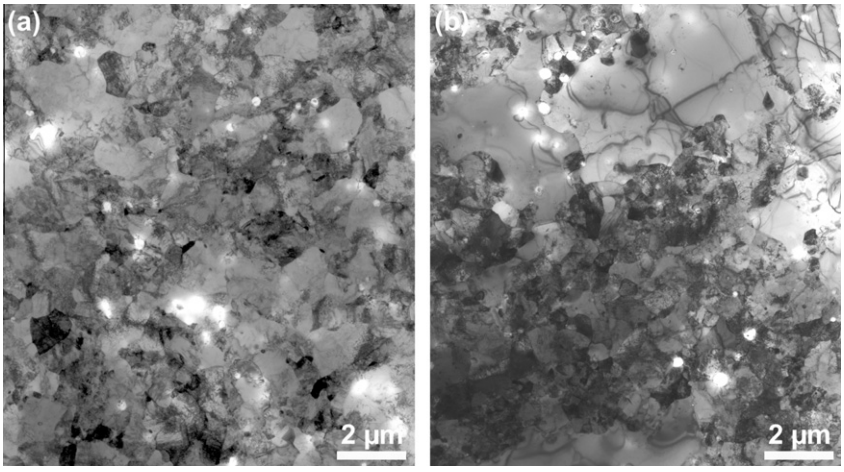

Fig. 3. TEM images showing the grain structure of the heat-treated: (a) Fe14CrY alloy and (b) Fe14CrYWTi alloy.

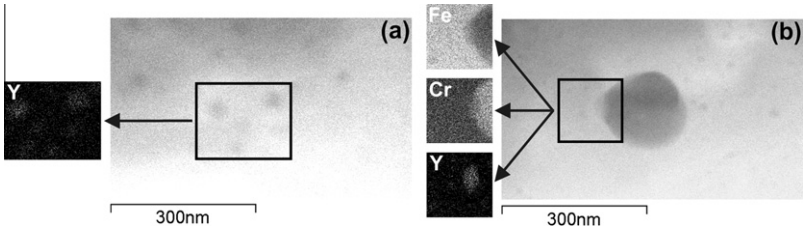

Fig. 4. (a) HAADF STEM image and Y XEDS map from the marked area showing the dispersion of nanoparticles in the heat-treated Fe14CrY alloy. (b) HAADF STEM image and Fe, Cr, Y XEDS maps from the marked area showing a Y-rich nanoparticle attached to a large Cr-rich particle in the heat-treated Fe14CrY alloy.

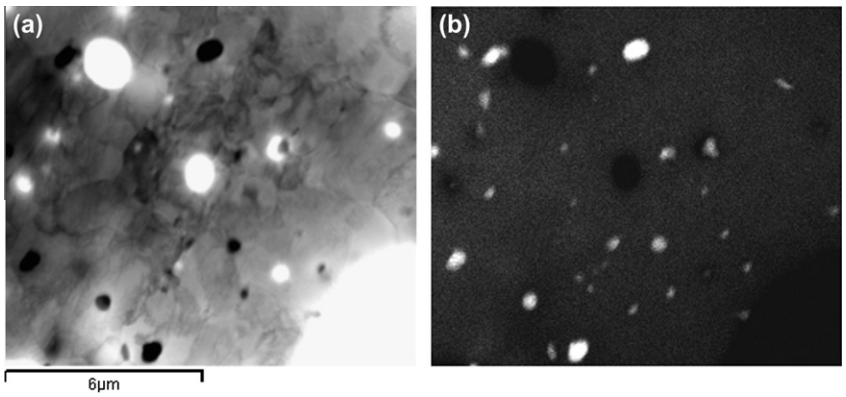

Fig. 5. Cr-rich particles in the heat-treated Fe14CrY alloy. (a) BF-STEM image of Cr-rich particles and (b) the corresponding STEM EDS Cr elemental map.

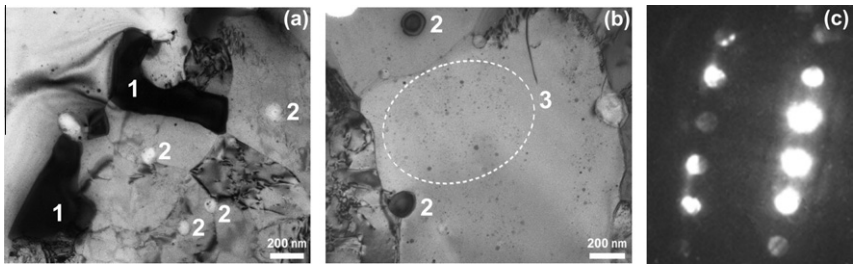

Fig. 6. TEM images of the heat-treated Fe14CrYWTi alloy showing (a) and (b) the three different types of second-phase particles. (c) Microdiffraction pattern indexed as $M_{23}C_6$ (M = Cr, W, Fe) oriented along the ⟨3 2 2⟩ zone axis from one type 1 particle in the heat-treated Fe14CrYWTi alloy.

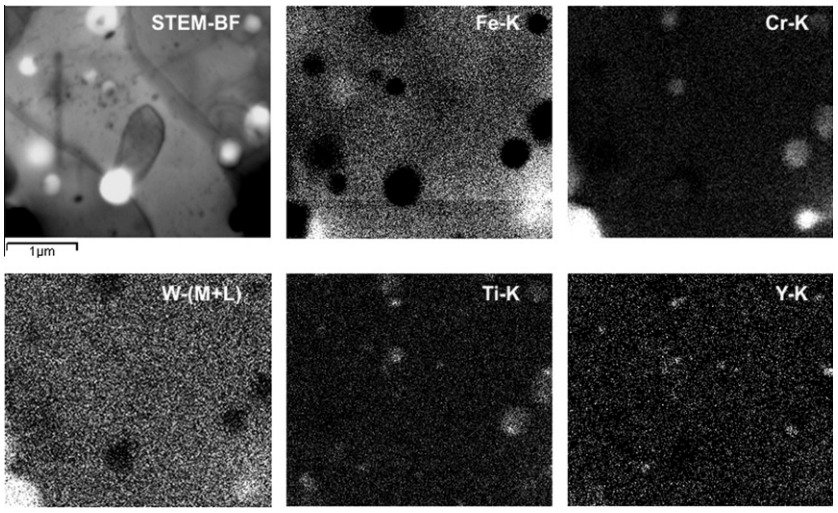

Fig. 7. STEM-BF image of the heat-treated Fe14CrYWTi alloy, and the corresponding elemental mapping images showing the composition of the second-phase particles.

Type 3 The most numerous particles, with round shape and sizes smaller than ~30 nm, and rather homogeneously distributed within the matrix grains as shown in Fig 6b. The size distribution and mean size of these particles were estimated by measuring more than 700 particles in different regions of the samples. Most of the particles had sizes below 10 nm. The mean number density of these particles resulted in $(8 \pm 2) \times 10^{21}$ cm ^{3} and their mean size 7 ± 5 nm. An estimation of the volume fraction of this type of particles in the alloy yielded a mean fraction of 0.4%. These particles contained Ti and Y as it is evident in the series of elemental mapping images shown in Fig. 7.

Attempts were made to identify the structure and composition of the Type 2 and Type 3 particles by analyzing accurate microdiffraction patterns from different particles having a suitable size. The analyses did not yield systematic or recurring results. Some particles of Type 2 could be identified as M_2O_3 (M = Cr, Ti) with an indexing uncertainty of 2.8% on a zone axis ⟨6 0 1⟩. But the same pattern was also indexed as corresponding to M_2O rutile (M = Ti, Cr) with an uncertainty of 3.6% on a zone axis ⟨3 1 5⟩. Others indexed as M_2O rutile did not match the M_2O_3 phase. Neither of the analyzed microdiffraction patterns from the Type 2 particles matched the M_3O_4 (M = Ti, Cr) phase nor Ti_2CrO_5. Respect to the

microdiffraction patterns from the Type 3 particles, it was found that only Y_2TiO_5 appeared to match the patterns from some particles with an indexing uncertainty of ~9%. The attempts for indexing the patterns from other particles failed to match the $Y_2Ti_2O_7$ and $YTiO_3$ phases, or any other of the expected phases.

The above results do not prove that nanoparticles of $Y_2Ti_2O_7$ and $YTiO_3$, or another phase different from Y_2TiO_5, have not formed in Fe14CrYWTi, but rather that the nanoparticles selected to be analyzed might very likely be just an aggregate of atoms; that is, their sizes are so small that the particles are essentially Y Ti O atom clusters or non stoichiometric oxide embryos. Then, a precise indexing of the diffraction patterns from these two forms should be rather problematical. It should be noted that the chemical composition and stoichiometry of the nanoprecipitates in the MA957 ODS ferritic alloy appears to be correlated with their sizes [14]. Previous TEM analyses performed on ODS steels containing O, Y and Ti have reported the presence of stoichiometric nanoparticles identified as $Y_2Ti_2O_7$ more frequently than as Y_2TiO_5 [14 16].

The quantitative EDS analyses in this alloy resulted in an average composition of 83.2%Fe 14.5%Cr 1.9%W 0.3%Ti 0.2%Y (wt.%) agreeing with the target composition of the alloy.

3.2. Tensile properties

The tensile properties of both alloys are summarized in Fig. 8. The yield strength and ultimate tensile stress for Fe14CrY at $T \leqslant 773$ K are significantly higher than the corresponding for Fe14CrYWTi. The opposite occurs above 773 K, the yield strength and the ultimate tensile stress for Fe14CrYWTi improve on the values for Fe14CrY by ~1.6 times. The uniform and total elongations for Fe14CrYWTi are higher over the temperature range studied except at 873 K where the elongation temperature curves for Fe14CrY exhibits a pronounced peak that is not observed for Fe14CrYWTi. It should be noted that an analogous peak in the elongation versus temperature has also been reported for the ODS Fe12Y and 12YWT steels, and for an extruded ODS alloy with the same composition than the Fe14CrYWTi alloy [17,18]. Moreover, the hardening ratio defined as the (ultimate tensile stress)/(yield strength) exhibits a very different behavior. It tends to decrease with increasing temperature for Fe14CrYWTi. In the case of Fe14CrY, the hardening ratio remains constant up to 773 K, increasing noticeably above this temperature from a value of ~1.08 1.35 at 973 K, exceeding the corresponding values for Fe14CrYWTi.

The differences in the microstructure of the alloys should cause the differences observed in the temperature behavior of the tensile properties, at least in major part. Then, the improved yield and tensile strengths above 773 K for Fe14CrYWTi appear to be due to the effectiveness of the Y Ti O nanoclusters for strengthening at high temperature. On the contrary, the dispersion of Y rich nanoparticles in Fe14CrY is apparently less effective, or ineffective, above 773 K. The superior yield and tensile strengths for the Fe14CrY

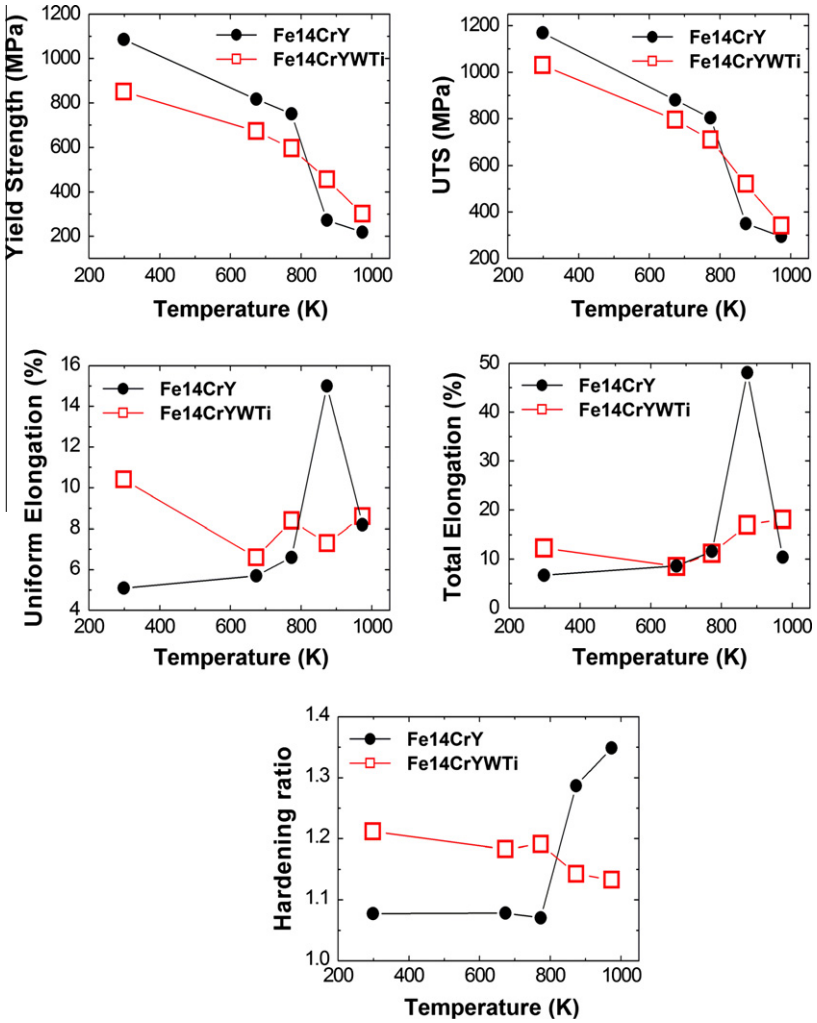

Fig. 8. Tensile properties as a function of temperature for the Fe14CrY and Fe14CrYWTi alloys heat-treated at 1123 K after forging.

alloy below this temperature could be an effect of the differences in the grain size and fraction of recrystallized material in the samples of the alloys. Grain size measurements and estimation of the recrystallized material fraction in the alloys were not accomplished because of the difficulty for resolving the grain structure properly due to the presence of a very high dislocation density and small unrecrystallized grains. However, it is very plausible that the Fe14CrY alloy heat treated after forging there had achieved a less recrystallized microstructure and more grain refinement than Fe14CrYWTi. It is important to remark that the above there might have occurred because Fe14CrYWTi, due to its high strength in the as HIP condition, had to be forged at ~50 K above the temperature used for Fe14CrY. The discrepancies between the temperature behavior of the mechanical properties for some commercial ODS steels and the ODS 12YWT alloy have been attributed to the effect of the grain size and recrystallized structure at low temperature, which is larger than that corresponding to dispersion strengthening [19].

4. Conclusions

Analytical TEM studies accomplished on Fe14CrY and Fe14CrYWTi ODS alloys revealed differences in the characteristics of the particle dispersions developed in these alloys. Second phase precipitates with sizes of ~1 μm were observed, and their compositions identified as Cr_2O_3 or $M_{23}C_6$ (M = Fe, Cr) in Fe14CrY, and as $M_{23}C_6$ (M = Cr, Fe, W) in Fe14CrYWTi. A dispersion of particles with sizes of less than ~30 nm was found in both alloys. In the case of the Fe14CrY alloy, these particles had a high Y content and some of them could be identified as $YCrO_3$. The corresponding dispersion in the Fe14CrYWTi alloy, which is apparently finer because the mean particle size was of 7 nm, consists of particles or atom clusters containing Y, Ti and O atoms. In particular, some particles were identified as Y_2TiO_5.

Moreover, a dispersion of Cr rich particles with sizes in the range ~50 500 nm appeared in the Fe14YCrWTi alloy. The electron diffraction pattern from several of these particles matched the structures either M_2O_3 or M_2O rutile (M = Cr, Ti). The sizes of these particles are in contrast with the larger sizes for the Cr_2O_3 particles in the Fe14CrY alloy, suggesting that Ti additions are effective for refining the M_2O_3 second phase particles in general.

The Fe14CrYWTi alloy, heat treated at 1123 K after forging, exhibits superior yield and tensile strengths at temperatures above 773 K in comparison with the counterpart Fe14CrY alloy. The opposite is found below this temperature. These differences in the temperature behavior of the tensile properties are attributed: (i) to a stronger dispersion strengthening effect of the Y Ti O clusters in the Fe14CrYWTi alloy compared with the one of the Y rich nanoparticles in Fe14CrY, and (ii) to a higher effectiveness of the low temperature strengthening mechanisms, i.e. grain boundary, dislocation and impurity hardening, in the case of the Fe14CrY alloy. This alloy exhibits a fine grained and unrecovered microstructure in contrast to the duplex grain structure found in Fe14CrYWTi with large recovered grains.

Acknowledgements

This investigation was supported by the Spanish Ministry of Science and Innovation (Project No. ENE 2008 06403 C06 04 and Juan de la Cierva program), the Comunidad de Madrid through the program ESTRUMAT CM (Grant S0505/MAT/0077), and the European Commission through the European Fusion Development Agreement (Contract No. 09 240), the IP3 FP6 ESTEEM project (Contract No. 026019) and the Fusion Energy Materials Science (FEMaS) FP7 coordination action. All the fundings are gratefully acknowledged.

References

[1] S. Ukai, M. Harada, H. Okada, M. Inoue, S. Nomura, S. Shikakura, K. Asabe, T. Nishida, M. Fujiwara, J. Nucl. Mater. 204 (1993) 65–73.
[2] M.J. Alinger, G.R. Odette, G.E. Lucas, J. Nucl. Mater. 307–311 (2002) 484–489.
[3] M.K. Miller, D.T. Hoelzer, E.A. Kenik, K.F. Russell, J. Nucl. Mater. 329–333 (2004) 338–341.
[4] D.T. Hoelzer, J. Bentley, M.A. Sokolov, M.K. Miller, G. Odette, M.J. Alinger, J. Nucl. Mater. 367–370 (2007) 166–172.
[5] N. Baluc et al., J. Nucl. Mater. 417 (2011) 149–153.
[6] V. de Castro, T. Leguey, M.A. Auger, S. Lozano-Perez, M.L. Jenkins, J. Nucl. Mater. 417 (2011) 217–220.
[7] D.J. Larson, P.J. Maziasz, I.S. Kim, K. Miyahara, Scripta Mater. 44 (2001) 359–364.
[8] M.K. Miller, E.A. Kenik, K.F. Russell, L. Heatherly, D.T. Hoelzer, P.J. Maziasz, Mater. Sci. Eng. A 353 (2003) 140–145.
[9] H. Kishimoto, M.J. Alinger, G.R. Odette, T. Yamamoto, J. Nucl. Mater. 329–333 (2004) 369–371.
[10] M.J. Alinger, G.R. Odette, D.T. Hoelzer, J. Nucl. Mater. 329–333 (2004) 382–386.
[11] M.K. Miller, K.F. Russell, D.T. Hoelzer, J. Nucl. Mater. 351 (2006) 261–268.
[12] The United Kingdom Chemical Database Service, D.A. Fletcher, R.F. McMeeking, D. Parkin, J. Chem. Inf. Comput. Sci. 36 (1996) 746–749.
[13] T. Malis, S.C. Cheng, R.F. Egerton, J. Electron Microsc. Tech. 8 (1988) 193–200.
[14] H. Sakasegawa, L. Chaffron, F. Legendre, L. Boulanger, T. Cozzika, M. Brocq, Y. de Carlan, J. Nucl. Mater. 384 (2009) 115118.
[15] I.S. Kim, J.D. Hunn, N. Hashimoto, D.L. Larson, P.J. Maziasz, K. Miyahara, E.H. Lee, J. Nucl. Mater. 280 (2000) 264–274.
[16] M. Klimiankou, R. Lindau, A. Möslang, J. Nucl. Mater. 329–333 (2004) 347351.
[17] R.L. Klueh, P.J. Maziasz, I.S. Kim, L. Heatherly, D.T. Hoelzer, N. Hashimoto, E.A. Kenik, K. Miyahara, J. Nucl. Mater. 307–311 (2002) 773–777.
[18] Z. Oksiuta, P. Olier, Y. de Carlan, N. Baluc, J. Nucl. Mater. 393 (2009) 114119.
[19] R.L. Klueh, J.P. Shingledecker, R.W. Swindeman, D.T. Hoelzer, J. Nucl. Mater. 341 (2005) 103114.